www.sciencemag.org/content/356/6335/291/suppl/DC1

Supplementary Materials for

iPTF16geu: A multiply imaged, gravitationally lensed type Ia supernova

A. Goobar,* R. Amanullah, S. R. Kulkarni, P. E. Nugent, J. Johansson, C. Steidel, D. Law, E. Mörtsell, R. Quimby, N. Blagorodnova, A. Brandeker, Y. Cao, A. Cooray, R. Ferretti, C. Fremling, L. Hangard, M. Kasliwal, T. Kupfer, R. Lunnan, F. Masci, A. A. Miller, H. Nayyeri, J. D. Neill, E. O. Ofek, S. Papadogiannakis, T. Petrushevska, V. Ravi, J. Sollerman, M. Sullivan, F. Taddia, R. Walters, D. Wilson, L. Yan, O. Yaron

*Corresponding author. Email: ariel@fysik.su.se

Published 21 April 2017, *Science* **356**, 291 (2017)
DOI: 10.1126/science.aal2729

This PDF file includes:

Materials and Methods

Supernova survey and follow-up

Between late August and December 2016, the intermediate Palomar Transient Factory (*34*) has been performing a mixed-cadence experiment on the 48-inch Samuel Oschin Telescope (P48) at the Palomar Observatory searching for transient phenomena, e.g., supernovae. About 100 fields ($\simeq 700$ square degrees in sky area) were observed every night, while another 200 fields were observed every three nights. During a night, each field was visited twice, with a one hour interval. For fields with available SDSS g-and Mould R-band (*35*) reference images, these two visits were one in each filter. For fields with only R-band reference images, these two visits were both in the R-band.

Images were transferred and processed by our real-time image subtraction pipeline at the National Energy Research Scientific Computing Center (*13*). This pipeline, equipped with high-performance computing and machine-learning transient classifiers (*36, 37*), delivered transient candidates for visual inspection by our duty astronomers within ten minutes of images being taken.

On 2016 Sep 11, our duty astronomer identified a transient candidate near the core of the galaxy SDSS J210415.89-062024.7 in one R-band-only one-day cadence field. This candidate was saved as iPTF16geu (a.k.a. SN2016geu) and put in the queue for spectroscopic classifica-

tion. However, iPTF16geu was not observed spectroscopically until Oct 2, as described below, and both the redshift and the transient type were unknown until that point.

Meanwhile the field was observed with a daily cadence in the R-band, as listed in Table S1. Difference imaging photometry in R-band was obtained using the iPTF Discovery Engine at the Infrared Processing and Analysis Center (*38, IDE*), where references images are aligned and matched to have the same point spread function (PSF) to the images where the SN is active. PSF photometry is then carried out and calibrated by matching the photometry of the field stars to the stellar catalog from the Sloan Digital Sky Survey (*21, SDSS*).

Complementary follow-up photometry, also listed in Table S1, was obtained in the $g'r'i'$-bands with the Rainbow Camera (RC) on the Spectral Energy Distribution Machine (*56, SEDM*) mounted on the Palomar 60-inch telescope (P60). For the redshift of iPTF16geu, $z_{SN} = 0.409$, these filters provide an excellent match to the rest-frame UBV filters (Fig. S1) that have historically been used for studying SNe Ia. The RC data was pre-processed following standard photometry reduction techniques. The host subtraction was done by using the automatic reference-subtraction photometry pipeline `FPipe` (*39*). This is using a similar approach to IDE, but images from the Sloan Digital Sky Survey are used as reference images of the host galaxy since such data is not available from the RC. The photometric uncertainty is determined as the measured scatter from placing artificial PSFs in a circular pattern around the real transient and measuring their values on the subtracted images. The P48 and P60 photometry is listed in Table S2. In the table, only the statistical uncertainty of each data point is quoted. The systematic uncertainties are all subdominant in this analysis, since the error on the derived magnification will be dominated by the intrinsic SN Ia brightness uncertainty.

SEDM is a Caltech-developed instrument, designed for fast transient classification and follow-up. The SEDM focal plane combines a photometric instrument, the RC, and an Integral Field Unit (IFU) spectrograph. The focal plane of the RC is split into four quadrants, each

one containing a SDSS generation 2 filter: $u'g'r'i'$. The field of view (FoV) is 6.5 arcmin^2 for each filter. The IFU, a lenslet array, is mounted in the center. The instrument covers the optical range 4000$-$9500 Å with a constant wavelength resolving power of $R \simeq$100, equivalent to a velocity resolution of 3000 km s^{-1}. Its FoV is 30 arcsec^2 and each spaxel covers an approximate diameter of $0.7''$. A spaxel is a spatial pixel that also contains a spectrum of its detected photons, which is characteristic for an IFU.

Spectroscopic follow-up

The first classification spectrum of iPTF16geu was obtained with the IFU on the SEDM on 2016 Oct 2. The combined spectrum (Fig. 1) consists of the average of two exposures, obtained with an offset of $10''$ to allow subtraction of the skylines. The data were reduced using a custom IFU pipeline developed for the instrument . Flux calibration and correction of telluric bands were done using the standard star BD+28 4211, which was taken at a similar airmass. An aperture of $4''$ was used to extract the spaxels. The details of all spectroscopic observations are listed in Table S3.

The classification and redshift of iPTF16geu from the low-resolution SEDM IFU spectrum was confirmed by observations obtained with the Double Spectrograph (*40, DBSP*) mounted on the Palomar 200-inch telescope (P200) and the ALFOSC instrument on the Nordic Optical Telescope (NOT).

For the DBSP observations the 600 lines/mm (with first order blaze wavelength 4000 Å) grating was used with slitwidths $1.5''$ and $2''$ and the data were reduced with a custom pipeline written in the Interactive Data Language (IDL). Flux calibration and telluric correction were done with the flux standard star BD+28 4211.

For the ALFOSC spectrum grism #4 was used with the slitwidth $1.0''$. The data were reduced with a custom pipeline written in Matlab. Wavelength calibration was performed with a He-Ne

arc lamp, and flux calibration with the standard star BD+17 4708 observed the same night at similar airmass.

Adaptive Optics observations of iPTF16geu

Natural Guide Star Adaptive Optics imaging from the VLT

K_s-band observations were obtained on 2016 Oct 11 using the Nasmyth Adaptive Optics System with the Near-Infrared Imager and Spectrograph (NACO) at the Very Large Telescope (VLT). The bright star at R.A.=$21^\circ 4' 17.42''$ and Dec=$-6^\circ 20' 43.13''$, $29.5''$ south-east of iPTF16geu with V =11.5 mag marked in Fig. 3, was used as a natural guide star (NGS). The spatial resolution decreases with the distance from the NGS, and $30''$ is close to the maximum distance for this technique. Due to problems with the visual wave-front sensor, the infrared wavefront sensor with the N20C80 dichroic was used. The observations were made with a standard jitter pattern in a $5''$ box with single exposure integrations of 20 s, saved in cube mode. In total, 348 frames were obtained. The data were reduced with the NACO `esorex` pipeline, using the standard jitter recipe (*41*). Since all exposures were individually saved, a small improvement in the final resolution could be obtained by selecting the best-resolved 20 % of the frames. The resulting image, Fig 3B, has an image quality of FWHM$\sim$0.3 $''$ at the location of the target, with a Strehl ratio of $\sim$5%. The Strehl ratio is defined as the ratio of peak diffraction intensities of an aberrated and a perfect wavefront. The ratio indicates the level of image quality in the presence of wavefront aberrations.

Laser Guide Star Adaptive Optics imaging from Keck

iPTF16geu was observed with the OSIRIS (*42*) imager behind the Keck I Laser Guide Star Adaptive Optics (LGSAO) system on 2016 Oct 13 and separately with the Keck II NIRC2 near-infrared imager in the H and K_s-bands (at 1.6 μm and 2.2 μm respectively) on 2016 Oct 22 and 23, and then again in the J-band (at 1.2 μm) on Nov 05. The field of view of the OSIRIS

imager is $20'' \times 20''$ and is sampled with $0.02''$ pixels by a 1024×1024 Hawaii 1 HgCdTe array. The observation consisted of a sequence of 36 exposures of 30 s each in the OSIRIS "$H_{\rm bb}$" filter (1.638/0.330 μm), dithered in a 3×3 box pattern with $2.5''$ separation. The NGS south-east of iPTF16geu mentioned above was used used for tip/tilt correction. Immediately following the iPTF16geu observation, the tip/tilt star was centered on the OSIRIS imager and a short sequence of dithered observations was taken as a PSF reference, yielding point source FWHM$\simeq 0.07''$ (as measured from the $H = 15$ mag star at R.A.$=21^{\circ}4'18.042''$ and Dec$=-6^{\circ}20'43.19''$ near the bright tip/tilt star).

The OSIRIS data were reduced using standard infrared self-calibration techniques. First, the 36 individual frames were scaled to a common median and combined into a super-sky frame using a 3-σ clipped mean algorithm, masking out a $2'' \times 2''$ box around the location of the target source in each frame. This super-sky was divided by its own median in order to produce a super-flat-field image that was then used to flat-field the individual science frames. The median unmasked value was then subtracted from each flat-fielded science frame in order to produce the flat-fielded, foreground-subtracted science frames. These frames were then shifted by the dither offsets (adjusted slightly by hand to ensure proper alignment) and combined using a 3-σ clipped mean algorithm. The final image is shown in Figures 3 and 4.

The NIRC2 observations consist of 39 exposures of 80 s each in the K_s-band, 9 exposures of 120 s each in the H-band and 5 exposures of 300 s each in the J-band. Unfortunately, for the J-band data, there was an instrument problem during the night and only two of the frames were used in the end. We used the same tip-tilt star as above to do the AO corrections. The observations were carried out using the NIRC2 narrow camera with a field of view of $100'' \times 100''$ and a pixel scale of $0.01''$/pixel. We dithered each of the frames by $2''$ using a custom nine-point dithering pattern for better sky subtraction. To correct for flat-fielding and dark currents we acquired a set of ten dark frames and twenty dome flat frames. The dome flats were separated

into two sets with the first half with the dome flat lamp off and second half with the lamp on. The dome flat off frames were used to estimate the thermal radiation which is non-negligible for the K_s-band. The dome flat on frames where then subtracted with the combined flat-off map, and the individual dark and flat frames where combined to generate master dark and dome flat frames, respectively. This produced a combined dark-subtracted and flat-fielded images in the J, H and K_s bands. For each science exposure the sky background of each pixel were estimated by using the preceding and following images after bad pixels and the object it self had been masked. The reduction was carried out using custom python scripts. The images were then finally corrected for geometric distortion using IDL routines available on the NIRC2 webpage.

The NIRC2 J-band, Fig. 4D, provides the highest resolution image in our dataset of the system where the four SN images are visible. We used this image to determine the SN positions by fitting a model to the system. The lensing galaxy was modeled using a Sérsic profile (*43*) while Gaussians were used for the the SN images. The fitted SN positions are shown in Table S4.

Observations with the Wide-Field Camera 3 aboard the Hubble Space Telescope

The Hubble Space Telescope (HST) Wide Field Camera 3 (WFC3) images presented in Fig. 4 A–C were obtained under program DD 14862 (Principal Investigator: Goobar) using the ultraviolet and visual (UVIS) channel on 2016 Oct 24 in the $F475W$, $F625W$ and $F814W$ filters (where the filter names correspond to the central wavelengths in nm). UVIS consists of two thinned, backside illuminated, ultra violet optimized 2048$\times$4096 pixel CCDs. However, only part of the UVIS2 chip was read for the iPTF16geu observations using the `UVIS2-C512C-SUB` aperture. UVIS has a pixel scale of $0.04''$/pixel and the diffraction limited PSF for these filters results in an image quality of FWHM$\simeq 0.07''$. We used a standard 3-point dithering pattern with post-flash to maximize the charge transfer efficiency (CTE) during read-out. The total expo-

sure time for the three filters were 378 s, 291 s and 312 s for $F475W$, $F625W$ and $F814W$, respectively.

The images were automatically processed at the Space Telescope Science Institute first through version 3.3 of the `calwf3` pipeline where they are dark subtracted, flat-fielded and corrected for charge-transfer inefficiency. Further, the individual flatfielded images were combined and corrected for geometric distortion using the `AstroDrizzle` software.

Using the same model as for the SN image positions, we fitted the relative fluxes of SN images 2–4 with respect to image 1. For this procedure we kept the image positions fixed to the values in Table S4, while allowing for a shift and a rotation of the the whole model. For the $F625W$ band, which covers a similar wavelength range as the R-band, we found that 90 % of the total flux is contained in images 1–2 and 70 % of the total flux is contained in image 1 alone. The relative brightnesses for the SN images with respect to the brightest image 1, the relative reddening, and the extinction these correspond to assuming the extinction law from (*23*) are shown in Table S5.

Fitting to a SN Ia lightcurve template

The lightcurves from the P48 and P60 photometry are presented in Figs. 2, and S2. Since SNe Ia are a homogenous class of objects, templates or lightcurve models can typically be fitted to the data. The free parameters are the time, t_0, and brightness, $m_B^\star$, of maximum in the rest-frame B-band, the lightcurve width and the color of the SN.

The lightcurve width can be quantified by introducing a stretch factor, s, that scales the time variable of the template with respect to t_0. It has been shown that same behavior is also captured by the second principal component of the SALT2 lightcurve model (*17*). In short, the SALT2 model is constructed from a principal component analysis of a large data set of normal SNe Ia. The eigenvalue for the first component is directly related to the peak brightness, $m_B^\star$, while the

eigenvalue for the second component, x_1, is normalized so that a SN with $x_1 = 0$ correspond to an average normal SN Ia. Further, objects with $x_1 = \pm 1$ have lightcurve widths that correspond to $\pm 1\sigma$ of normal SNe Ia lightcurve width distribution.

The color is typically defined in terms of the rest-frame $B - V$ magnitude. This is then used to scale a color, or extinction, law that describes how the flux ratios vary with wavelength. For a standard extinction law, the color excess, $E(B - V)$, is used to scale the law, where $E(B - V)$ is the $B - V$ magnitude deviation from what would have been measured in the absence of extinction. SALT2 uses an empirically derived color law where the scaling parameter, $\mathcal{C}$, is the deviation from the average $B - V$ rest-frame color.

We fitted both a lightcurve template and the SALT2 model to the P48 and P60 photometry. In Fig. 2 we show the best fitted SALT2 model. SALT2 was also used for the SN Ia cosmology sample presented in (*20*). Using the same model allows us to estimate the magnification independently of the value of the Hubble constant, H_0, or any other cosmological parameter. The SALT2 model has four free parameters, for which we obtain, $t_0 = 57654.1 \pm 0.2$, $m_B^\star = 19.12 \pm 0.03$, and $\mathcal{C} = 0.23 \pm 0.03$ and $x_1 = 0.08 \pm 0.19$, respectively. The corrected peak magnitude, $m_B^{\rm corr}$, is further obtained as

$$m_B^{\rm corr} = m_B^\star - \beta \cdot \mathcal{C} + \alpha \cdot x_1$$

where $\beta = 3.101 \pm 0.075$ and $\alpha = 0.141 \pm 0.006$ have been derived simultaneously with the cosmological parameters by (*20*) from the full sample of 740 SNe Ia. Since their data set is well-sampled around $z = 0.4$, we can compare the lightcurve of iPTF16geu with the expected average for the same redshift. This is shown in Fig. 2 together with the intrinsic brightness dispersions of SNe Ia. By then comparing the derived peak magnitude of iPTF16geu with the expected for an unlensed SN Ia at $z = 0.409$, we find that the SN has been boosted by -4.3 ± 0.2 magnitudes where the intrinsic dispersion is accounted for in the quoted error bar.

We also tried to fit the spectral series of SN 2011fe, which is a normal and well observed SN Ia, to the data. In Fig. S2 we show both the SALT2 lightcurve model and the best SN 2011fe fit using the spectral series for the latter compiled by (*44*). The data are perfectly consistent with both models but SN 2011fe provides a better fit in the rest-frame U-band. However, since the SALT2 fit allows us to directly compare the brightness of iPTF16geu to other SNe Ia at the same redshift in a cosmology independent manner we decided to use this for the main analysis. iPTF16geu has the same lightcurve shape as SN2011fe, but a reddening of $E(B-V) = 0.31 \pm 0.05$ mag is required, assuming the extinction law from (*23*).

Both the SALT2 model and SN 2011fe fits show that the iPTF16geu is consistent with a normal and average SNe Ia, but the derived values of $\mathcal{C}$ and $E(B-V)$ suggest that that the SN is reddened by interstellar extinction. This reddening is taken into account for the estimated lensing magnification and uncertainty above. However, given that most of the measured light, $\sim 70\,\%$, is contained in SN image 1, the measured $\mathcal{C}$ is dominated by the color of this image. Since we have also measured differential reddening of images 2–4 with respect to SN image 1, the magnification of the system could in fact be higher. If the measured differential extinction from Table S5 is taken into account we find that the total magnification of the system lie in the range -4.1 mag to -4.8 mag.

Modelling of the gravitational lens

Our default lens model is an isothermal ellipsoid galaxy (*25, 26*) for which the convergence is given by

$$\kappa = \frac{b}{2\omega}, \tag{S1}$$

where b is a convergence normalization parameter and

$$\omega^2 = (1-\epsilon)(x-x_0)^2 + (1+\epsilon)(y-y_0)^2. \tag{S2}$$

Here, x_0 and y_0 correspond to the position of the lens centre and $(1+\epsilon)/(1-\epsilon)$ is the major-to-minor axis ratio. The magnification is given by (*26*)

$$\mu(x_1, x_2) = \left(1 - \frac{b}{\omega}\right)^{-1}, \tag{S3}$$

i.e., the isodensity contour $\kappa = 1/2$ correspond to the critical line in the lens plane. In the forthcoming, positions in the lens plane are given in angular units. In terms of ϵ, the ellipticity, ϵ_e, of the galaxy is given by

$$\epsilon_e = 1 - \sqrt{\frac{1-\epsilon}{1+\epsilon}}. \tag{S4}$$

The projected mass M inside an isodensity contour of constant ω is given by (*26*)

$$M = \frac{c^2}{4G}\frac{D_s D_l}{D_{ls}}\frac{b\omega}{\sqrt{1-\epsilon^2}}. \tag{S5}$$

Assuming cosmological parameter values of $H_0 = 67.8$ km s^{-1}Mpc^{-1} and $\Omega_M = 0.308$ and zero spatial curvature (*45*),

$$D_l = 745.8\,\mathrm{Mpc}, D_s = 1157.0\,\mathrm{Mpc}, \text{and } D_{ls} = 513.2\,\mathrm{Mpc},$$

where D_l is the angular diameter distance to the lens, D_s to the source and D_{ls} between the lens and the source. The mass inside the critical line where $\omega = b$ is

$$M = \left(\frac{b}{1''}\right)^2 \frac{2.0 \cdot 10^{11}\, M_\odot}{\sqrt{1-\epsilon^2}}. \tag{S6}$$

Using the `lensmodel` software (*46, 47*), we fit the model to the observed SN positions by varying b, ϵ, the position angle ϕ (from from North to East) of the major axis, and the offset, $(\Delta\alpha, \Delta\delta)$, between the center of the lens model and the Sérsic profile used to fit the observed light of the lensing galaxy as described above. The results are

$$\begin{aligned} b &= 0.287'' \pm 0.005'', \\ \Delta\alpha &= -0.013'' \pm 0.007'', \end{aligned}$$

$$\begin{aligned}\Delta\delta &= -0.004'' \pm 0.008'',\\ \epsilon &= 0.16 \pm 0.09,\\ \phi &= 65.8 \pm 0.9,\end{aligned}$$

or

$$M = (1.69 \pm 0.06) \cdot 10^{10}\, M_{\odot}, \tag{S7}$$

$$\epsilon_e = 0.15 \pm 0.07. \tag{S8}$$

For the best fit parameter values we get $\chi^2_{\rm min} = 0.022$. Constraining the centre of the lens to coincide with the maximum surface brightness of the lens galaxy, i.e. $(\Delta\alpha, \Delta\delta) = (0, 0)$ within the observational uncertainties, i.e., $\pm\, 0.008''$, the minimum χ^2 increases to $\chi^2_{\rm min} = 1.8$. Following (*30*), we calculate the velocity dispersion by averaging over all possible inclination angles and intrinsic axis ratios that can give rise to the observed projected surface density. The resulting relation between b and the velocity dispersion, σ_v, is given by

$$b = 4\pi \left(\frac{\sigma_v^2}{c^2}\right)^2 \frac{D_{ls}}{D_s} \sqrt{1-\epsilon}\lambda \left(\sqrt{\frac{1-\epsilon}{1+\epsilon}}\right), \tag{S9}$$

where the functional form of λ depends on the probability for the three dimensional mass distribution of the lens to be oblate or prolate. Assuming total ignorance of this probability, we can read off the value of λ for $\epsilon = 0.16$ from figure 1 in (*30*) to be $\lambda = 1 \pm 0.05$. Numerically, we have

$$\sigma_v = 280 \left(\tfrac{b}{\lambda}\sqrt{1-\epsilon}\right)^{\frac{1}{2}}\ {\rm km\,s^{-1}} = 156 \pm 4\,{\rm km\,s^{-1}},$$

where $\lambda\sqrt{1-\epsilon} = 0.92 \pm 0.04$.

We calculate the expected flux ratios, r, and their associated uncertainties by taking a weighted average of the flux ratios over a grid of parameter values, here denoted by index

i,

$$\bar{r} = \sum_i \mathcal{L}_i r_i, \tag{S10}$$

$$\sigma_{\bar{r}}^2 = \sum_i \mathcal{L}_i (r_i - \bar{r})^2, \tag{S11}$$

where the weight is given by the likelihood of the parameter values given the observed image positions,

$$\mathcal{L}_i \equiv \exp\left(-\frac{1}{2}\chi_i^2\right) / \sum_i \exp\left(-\frac{1}{2}\chi_i^2\right). \tag{S12}$$

Suppressing the bar as an indicator for average values, the magnitude differences $\Delta m_{ij} = -2.5 \ln f_i/f_j$ between images i and j are:

$$\begin{array}{lll} \Delta m_{12} = -0.39 \pm 0.11, & \Delta m_{13} = -0.33 \pm 0.06, & \Delta m_{14} = 0.73 \pm 0.06, \\ \Delta m_{23} = \quad 0.04 \pm 0.11, & \Delta m_{24} = \quad 1.11 \pm 0.06, & \Delta m_{34} = 1.06 \pm 0.06. \end{array}$$

In conclusion, image 4 is expected to be the brightest, while it is in fact observed to be the faintest.

The predicted time delay, calculated as weighted averages analogously to the flux ratios, between the SN images is small, ranging from 1.9 ± 1.2 hours to 15.7 ± 6.3 hours. Thus, the maximal time-delay between any two images is 35 hours at the 99.9% confidence level with the adopted model.

While the model estimates of the magnitude differences among the SN images have small uncertainties, the total magnification is poorly constrained. Since there is a tail of very high magnification output compatible with the observed image positions, the resulting weighted mean total magnification is very sensitive to details of the grid of parameter values and possible cuts of low probability parameter values. Only when disregarding all parameter values not being within 2σ of the best fit parameters can the total magnification be constrained at all, $\mu_{\rm tot} = 43 \pm 29$, consistent with the observed magnification $\mu \sim 52$.

Motivated by the discrepancy between the image magnitude differences observed and the ones predicted by the smooth lensing model, we consider the possibility of sub-structures as possible added contributors to the lensing of one or more SN images.

Such sub-structures can include galactic subhalos (*52*), and compact objects in the form of stars or possible compact dark matter objects. The magnification of SNe from stars is studied in (*53*), where it is found that $\sim 70\,\%$ of multiple lensed SNe will experience additional magnification from the lens galaxy star population of > 0.5 mag. The case of lensed quasars is studied in, e.g (*54*).

A population of compact objects will create a network of caustics that can give rise to large magifications if the source size is sufficiently small. If there is a relative motion between the source, observer and the lensing compact object, or if the source size is changing, the magnification can vary. The time scale of the variations will typically correspond to the Einstein radius crossing time (see below), but can also be shorter in the case of caustic crossing events (*55*).

A full treatment of the gravitational lensing effects of sub-structures is beyond the scope of this paper, but in order to show the typical scales involved, we briefly study the lensing effect of a single compact object.

In the isolated point mass lens approximation, the relevant source plane length scale is given by (*48*)

$$\eta_0 = \sqrt{2R_S \frac{D_s D_{ls}}{D_l}} = \sqrt{\frac{M}{M_\odot}} \times 3.8 \cdot 10^{16}\,\mathrm{cm}, \tag{S13}$$

where R_S is the Schwarzschild radius of the lens. To act efficiently as a lens, η_0 should be larger than the physical size, R, of the Type Ia SNe photosphere, typically

$$\frac{R}{10^{15}\,\mathrm{cm}} \sim 2.0 + 0.62 \frac{(t - t_{\max})}{1\,\mathrm{week}}\,, \tag{S14}$$

which is derived from the the measured expansion velocities of the photosphere of SN2011fe (*22, 49*).

A single lens point mass should have $M \gtrsim 0.12 M_{\odot}$ to be effective also one month after maximum. For a lens with velocity 156 km s^{-1}, this corresponds to time scales greater than 9 years. We can thus neglect any time dependence induced to the lightcurve from the motion of isolated point masses with $M \gtrsim 0.12 M_{\odot}$.

Predicted rate of highly magnified SNe Ia in iPTF

To date, almost 2000 SNe Ia up to $z \sim 0.2$ have been discovered at P48 and classified over a period of eight years (945 observing nights), with a detection limit of $R \sim 21$ mag. Since they are brighter, lensed SNe can be observed to higher redshifts. Using the compilation of measured SN Ia volumetric rates in (*1,* see their Fig. 2), we estimate that within the larger volume up to $z = 0.4$, the number of SNe Ia explosions is 12.6 deg^{-2} year^{-1}, which when combined with the total monitoring time and the average solid angle of the survey, yields a total of 6×10^4 SNe Ia in the field of view. This corresponds to a relative fraction 1.7×10^{-5} for events like iPTF16geu, if this single event is representative for the true rate. Estimates of the inefficiencies in transient detection and spectroscopic typing over the lifetime of the survey have been included in the calculation.

To compare this outcome with the estimate of the expected probability we use the ray-tracing SNOC Monte-Carlo package (*50*). SNOC was used in (*11*) to assess the expected rate of strongly lensed SNe in planned satellite missions. We run a total of 10^7 simulated lines-of-sight up to $z = 0.45$, with a volumetric redshift dependent SN Ia rate following the star formation rate with redshift, one of the options in SNOC. The matter spatial distribution in galaxy halos along the line of sight are simulated with two different smooth spherical functions, the Singular Isothermal Sphere (SIS) profile,

$$\rho(r) = \frac{\sigma_v^2}{2\pi G r^2},$$

where σ_v^2 is the velocity dispersion; and the NFW profile (*51*),

$$\rho(r) = \frac{\rho_0}{\frac{r}{R_s}\left(1+\frac{r}{R_s}\right)^2},$$

where ρ_0 and R_s parameters of the model and vary between halos. Since we only consider spherical profiles, our simulations will not produce four, but only two images. Furthermore, these simulations do not include the contribution from microlensing by a stellar population in the line of sight.

However, in addition to the smooth spherical functions, we tested adding contributions from point-like lenses (POI) to the mass density. In all cases, the contributions to the mass density is self-consistently normalised to give the cosmological average mass density of the universe found by the Planck collaboration for a ΛCDM universe, $\Omega_M = 0.308$ (*45*). The resulting distribution of the expected gravitational lensing amplification for the iPTF survey, μ, can be seen in Fig. S3. For the simulations with smooth distributions, e.g., NFW, no event like iPTF16geu came out of the simulations, corresponding to a probability less than 10^{-3} . Adding substructures in the from of compact objects increases the chances of intersecting a lens, yet the high magnification found for iPTF16geu is rare. For a 90% contribution of compact objects to the cosmic mass density, Ω_M, we find a 5% chance of discovering a SN Ia with comparable lensing magnification within the limited redshift range probed. In conclusion, the lensing characteristics of iPTF16geu are rather unlikely, even considering the possibility of having a high density of discrete compact sources.

Table S1: **Imaging of iPTF16geu.** All observations where imaging data of iPTF16geu were obtained.

UTC Civil date	MJD (days)	Telescope	Filter	Exp. time (s)
2016 Sep 05.3	57636.33	P48	R	60
2016 Sep 06.2	57637.18	P48	R	120

Continued on next page

UTC Civil date	MJD (days)	Telescope	Filter	Exp. time (s)
2016 Sep 07.2	57638.18	P48	R	120
2016 Sep 08.2	57639.23	P48	R	120
2016 Sep 09.2	57640.21	P48	R	120
2016 Sep 10.2	57641.20	P48	R	120
2016 Sep 11.2	57642.20	P48	R	120
2016 Sep 15.3	57646.33	P60/RC	r'	90
2016 Sep 15.3	57646.33	P60/RC	i'	90
2016 Sep 15.3	57646.33	P60/RC	g'	90
2016 Sep 17.4	57648.36	P60/RC	r'	90
2016 Sep 17.4	57648.36	P60/RC	i'	90
2016 Sep 17.4	57648.36	P60/RC	g'	90
2016 Sep 23.1	57654.14	P48	R	60
2016 Sep 24.1	57655.11	P48	R	120
2016 Sep 25.1	57656.12	P48	R	120
2016 Sep 26.1	57657.15	P48	R	120
2016 Sep 27.1	57658.13	P48	R	120
2016 Sep 28.2	57659.25	P48	R	60
2016 Sep 29.1	57660.15	P48	R	60
2016 Sep 30.1	57661.11	P48	R	120
2016 Oct 01.1	57662.10	P48	R	120
2016 Oct 02.1	57663.12	P48	R	120
2016 Oct 03.2	57664.17	P48	R	60
2016 Oct 03.2	57664.25	P60/RC	r'	90
2016 Oct 03.3	57664.25	P60/RC	i'	90
2016 Oct 03.3	57664.26	P60/RC	r'	90
2016 Oct 03.3	57664.26	P60/RC	i'	90
2016 Oct 03.3	57664.26	P60/RC	g'	90
2016 Oct 04.3	57665.29	P60/RC	r'	90
2016 Oct 04.3	57665.30	P60/RC	i'	90
2016 Oct 04.3	57665.30	P60/RC	g'	90
2016 Oct 06.1	57667.11	P60/RC	r'	90
2016 Oct 07.1	57668.10	P48	R	120
2016 Oct 08.1	57669.11	P48	R	60
2016 Oct 08.1	57669.15	P60/RC	r'	90
2016 Oct 09.1	57670.10	P48	R	60
2016 Oct 09.2	57670.17	P60/RC	r'	90
2016 Oct 09.2	57670.17	P60/RC	i'	90
2016 Oct 09.2	57670.17	P60/RC	g'	90
2016 Oct 09.2	57670.22	P60/RC	r'	90
2016 Oct 09.2	57670.23	P60/RC	i'	90
2016 Oct 10.2	57671.22	P60/RC	i'	90
2016 Oct 10.2	57671.24	P60/RC	r'	90
2016 Oct 10.2	57671.24	P60/RC	i'	90
2016 Oct 11.1	57672.05	VLT/NACO	K_s	6960
2016 Oct 12.2	57673.19	P60/RC	r'	90
2016 Oct 12.2	57673.19	P60/RC	i'	90

Continued on next page

UTC Civil date	MJD (days)	Telescope	Filter	Exp. time (s)
2016 Oct 12.2	57673.21	P60/RC	r'	90
2016 Oct 12.2	57673.21	P60/RC	i'	90
2016 Oct 13.1	57674.12	P60/RC	r'	90
2016 Oct 13.1	57674.12	P60/RC	i'	90
2016 Oct 13.2	57674.21	Keck/OSIRIS	$H_{\rm bb}$	1080
2016 Oct 13.2	57674.21	P60/RC	r'	90
2016 Oct 13.2	57674.21	P60/RC	i'	90
2016 Oct 22.2	57683.22	Keck/NIRC2	K_s	3120
2016 Oct 23.2	57684.22	Keck/NIRC2	H	1080
2016 Oct 24.9	57685.88	HST/WFC3	$F625W$	291
2016 Oct 24.9	57685.89	HST/WFC3	$F814W$	312
2016 Oct 24.9	57685.92	HST/WFC3	$F475W$	378
2016 Nov 05.2	57697.21	Keck/NIRC2	J	600

Table S2: **Photometry of individual exposures of iPTF16geu from the P48 and P60/RC observations listed in Table S1. The photometry is given in flux, f, which can be converted to magnitudes, m, in the AB system as $m = -2.5\log_{10}(f) + ZP$, with $ZP = 25$.**

UTC Civil date	MJD (days)	Telescope	Filter	Flux (arbitrary)	Flux σ	ZP (AB)
2016 Aug 31.3	57631.33	P48	R	19	10	25.0
2016 Sep 01.3	57632.32	P48	R	8	13	25.0
2016 Sep 02.4	57633.35	P48	R	17	8	25.0
2016 Sep 04.3	57635.33	P48	R	38	10	25.0
2016 Sep 05.3	57636.33	P48	R	52	10	25.0
2016 Sep 06.2	57637.18	P48	R	81	13	25.0
2016 Sep 06.3	57637.33	P48	R	84	12	25.0
2016 Sep 07.2	57638.18	P48	R	98	11	25.0
2016 Sep 07.3	57638.33	P48	R	86	11	25.0
2016 Sep 08.2	57639.23	P48	R	115	14	25.0
2016 Sep 08.3	57639.34	P48	R	110	10	25.0
2016 Sep 09.2	57640.21	P48	R	131	13	25.0
2016 Sep 09.3	57640.32	P48	R	131	13	25.0
2016 Sep 10.2	57641.20	P48	R	166	18	25.0
2016 Sep 10.3	57641.32	P48	R	153	13	25.0
2016 Sep 11.2	57642.20	P48	R	205	19	25.0
2016 Sep 11.3	57642.31	P48	R	177	18	25.0
2016 Sep 15.3	57646.33	P60/RC	r'	221	16	25.0
2016 Sep 15.3	57646.33	P60/RC	i'	278	10	25.0
2016 Sep 15.3	57646.33	P60/RC	g'	107	13	25.0
2016 Sep 17.4	57648.36	P60/RC	r'	270	37	25.0
2016 Sep 17.4	57648.36	P60/RC	i'	325	18	25.0

Continued on next page

UTC Civil date	MJD (days)	Telescope	Filter	Flux (arbitrary)	Flux σ	ZP (AB)
2016 Sep 17.4	57648.36	P60/RC	g'	112	16	25.0
2016 Sep 23.1	57654.14	P48	R	288	19	25.0
2016 Sep 24.1	57655.11	P48	R	283	23	25.0
2016 Sep 24.2	57655.24	P48	R	283	18	25.0
2016 Sep 25.1	57656.12	P48	R	310	23	25.0
2016 Sep 25.2	57656.25	P48	R	278	20	25.0
2016 Sep 26.1	57657.15	P48	R	273	18	25.0
2016 Sep 26.2	57657.25	P48	R	270	25	25.0
2016 Sep 27.1	57658.13	P48	R	281	21	25.0
2016 Sep 27.2	57658.18	P48	R	273	18	25.0
2016 Sep 28.2	57659.25	P48	R	286	24	25.0
2016 Sep 29.1	57660.15	P48	R	251	21	25.0
2016 Sep 30.1	57661.11	P48	R	247	20	25.0
2016 Sep 30.2	57661.15	P48	R	231	19	25.0
2016 Oct 01.1	57662.10	P48	R	265	27	25.0
2016 Oct 01.2	57662.23	P48	R	238	18	25.0
2016 Oct 02.1	57663.12	P48	R	227	17	25.0
2016 Oct 02.2	57663.22	P48	R	225	19	25.0
2016 Oct 03.2	57664.17	P48	R	229	19	25.0
2016 Oct 03.2	57664.25	P60/RC	r'	223	18	25.0
2016 Oct 03.3	57664.25	P60/RC	i'	347	29	25.0
2016 Oct 03.3	57664.26	P60/RC	r'	236	13	25.0
2016 Oct 03.3	57664.26	P60/RC	i'	316	55	25.0
2016 Oct 03.3	57664.26	P60/RC	g'	48	8	25.0
2016 Oct 04.3	57665.29	P60/RC	r'	205	19	25.0
2016 Oct 04.3	57665.30	P60/RC	i'	319	91	25.0
2016 Oct 04.3	57665.30	P60/RC	g'	53	8	25.0
2016 Oct 06.1	57667.11	P60/RC	r'	192	37	25.0
2016 Oct 07.1	57668.10	P48	R	203	19	25.0
2016 Oct 07.2	57668.22	P48	R	191	18	25.0
2016 Oct 08.1	57669.11	P48	R	180	23	25.0
2016 Oct 08.1	57669.15	P60/RC	r'	145	27	25.0
2016 Oct 09.1	57670.10	P48	R	194	25	25.0
2016 Oct 09.2	57670.17	P60/RC	r'	163	6	25.0
2016 Oct 09.2	57670.17	P60/RC	i'	251	12	25.0
2016 Oct 09.2	57670.17	P60/RC	g'	25	4	25.0
2016 Oct 09.2	57670.22	P60/RC	r'	146	12	25.0
2016 Oct 09.2	57670.23	P60/RC	i'	244	52	25.0
2016 Oct 10.2	57671.22	P60/RC	i'	227	368	25.0
2016 Oct 10.2	57671.24	P60/RC	r'	126	13	25.0
2016 Oct 10.2	57671.24	P60/RC	i'	242	187	25.0
2016 Oct 12.2	57673.19	P60/RC	r'	120	135	25.0
2016 Oct 12.2	57673.19	P60/RC	i'	223	29	25.0
2016 Oct 12.2	57673.21	P60/RC	r'	118	13	25.0
2016 Oct 12.2	57673.21	P60/RC	i'	256	141	25.0
2016 Oct 13.1	57674.12	P60/RC	r'	132	18	25.0
2016 Oct 13.1	57674.12	P60/RC	i'	203	11	25.0

Continued on next page

UTC Civil date	MJD (days)	Telescope	Filter	Flux (arbitrary)	Flux σ	ZP (AB)
2016 Oct 13.2	57674.21	P60/RC	r'	96	12	25.0
2016 Oct 13.2	57674.21	P60/RC	i'	238	79	25.0

Table S3: **Spectroscopic observations of iPTF16geu used for identification and redshift measurements.**

UT Date	MJD (days)	Phase (days)	Telescope Instrument	R ($\lambda/\Delta\lambda$)	$\Delta\lambda$ (Å)	λ range (Å)	Exp. time (s)	Airmass
Oct 2.23	57663.23	6.5	P60/SEDM	100	58	4000-9500	2700	1.43
Oct 4.22	57665.22	7.9	P200/DBSP	740	8	3300-10000	1800	1.37
Oct 6.13	57667.13	9.3	P200/DBSP	560	10	3300-10000	3600	1.51
Oct 9.90	57670.90	12.0	NOT/ALFOSC	360	16	3500-9600	2700	1.22

Table S4: **Fitted relative SN image positions.** The positions are given in polar coordinates with respect to the center, of the Sérsic profile, and the angle, $-\pi < \phi \leq \pi$, is defined from West to North. The SN image numbers are shown in Fig. 4. The fitted statistical uncertainty on r and are ϕ $0.001''$ and 0.004 rad, respectively. The uncertainty, in the position of the whole system, i.e. the center of the Sérsic profile is $0.008''$ in both x and y.

SN Image	r (arcsec)	ϕ (rad)
1	0.2679	$+1.7861$
2	0.3133	-2.7252
3	0.2874	-0.9761
4	0.2803	$+0.4554$

Table S5: **Relative photometry with respect to the first SN image**. Here, $E(F625W - F814W)$, is the relative color color excess with respect to SN image 1. All quoted uncertainties are statistical errors. In the last two columns, the relative extinction are given using the measured $E(F625W - F814W)$ together with the extinction law from (*23*).

SN image	$\Delta F625W$ (mag)	$\Delta F814W$ (mag)	$E(F625W - F814W)$ (mag)	A_{F625W} (mag)	A_{F814W} (mag)
2	$1.26(0.01)$	$1.12(0.01)$	$0.14(0.01)$	0.5	0.4
3	$2.46(0.02)$	$2.33(0.02)$	$0.12(0.03)$	0.5	0.4
4	$3.62(0.05)$	$2.88(0.03)$	$0.75(0.06)$	2.8	2.1

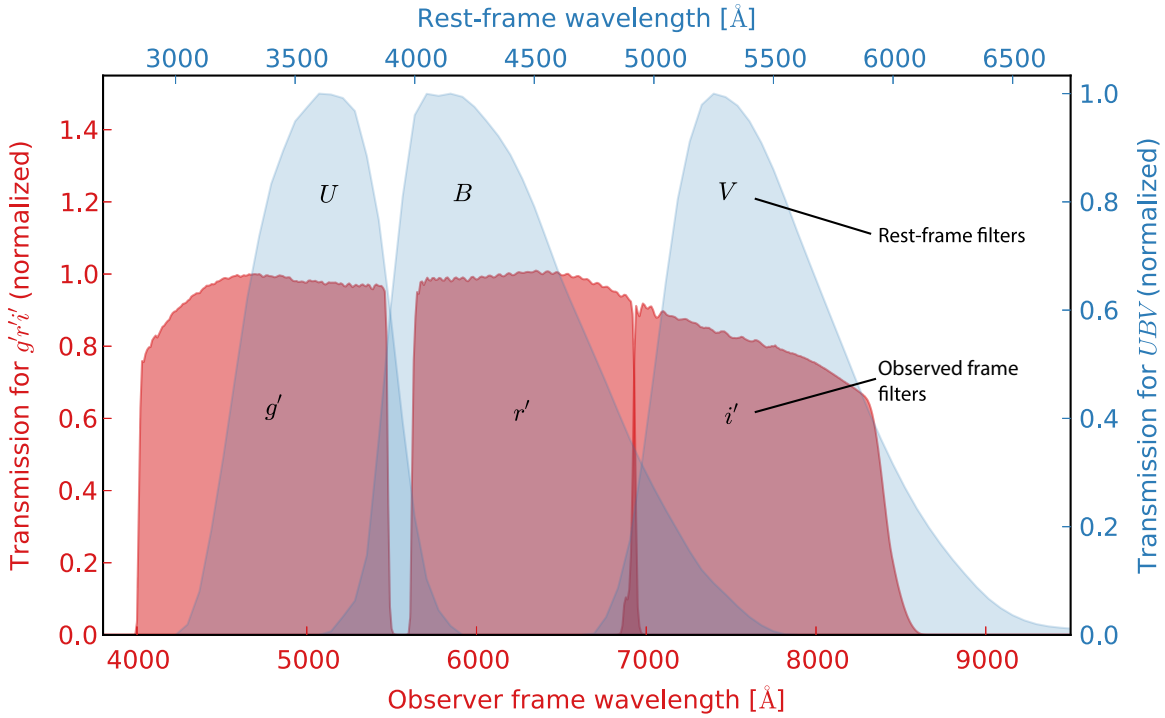

Figure S1: **Comparison between the observer frame P60 RC filters and the rest-frame standard filters UBV, which historically have been used for studying SNe Ia.**. The relative transmissions of the observer frame P60 $g'r'i'$ filters are shown in red for the wavelengths indicated by the bottom horizontal axis, while the corresponding rest-frame wavelengths and UBV filter transmissions are plotted in blue. It is clear from the figure that the observer frame RC $g'r'i'$ filters provide a close match to the rest-frame UBV for the redshift $z_{SN} = 0.409$.

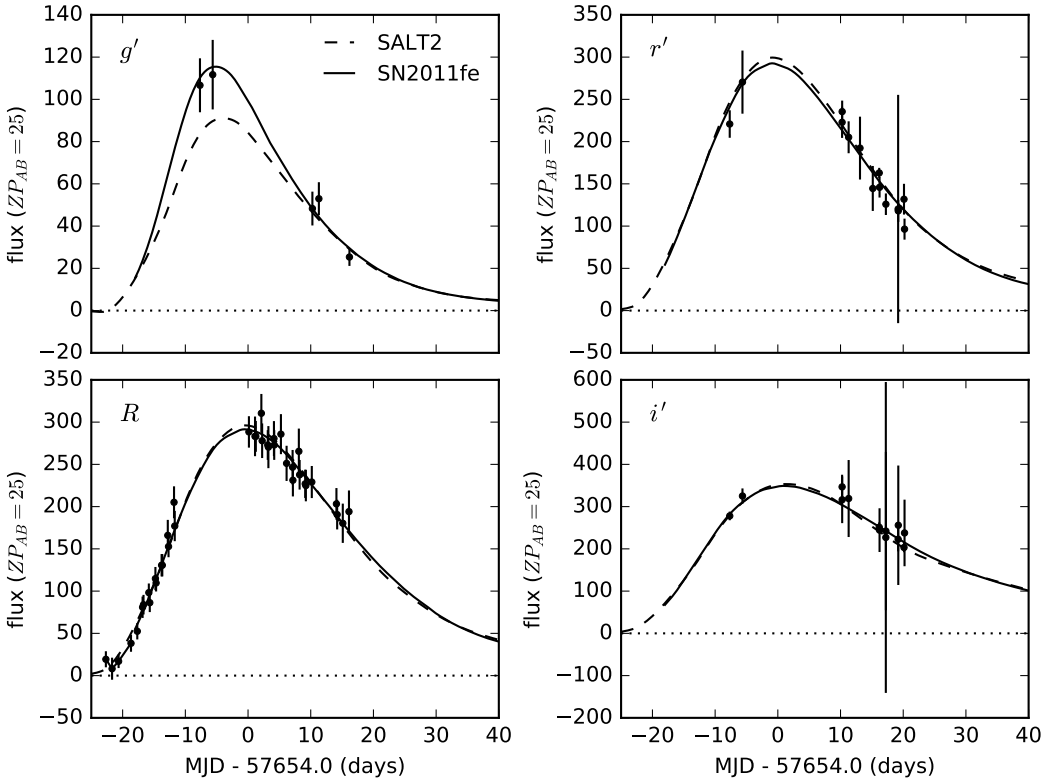

Figure S2: **Lightcurves of iPTF16geu in the P48 R-band and the P60 RC $g'r'i'$ bands.** The error bars are correlated. The solid lines show the fit of the nearby and normal SN 2011fe, while the dashed show the best fit using the SALT2 model. The lightcurve fitting is carried out in linear flux space which appropriately allows the inclusion of low signal-to-noise and negative flux measurements. These points have been omitted in the plotting of Fig. 2, which is shows magnitudes, while all data are shown here. The individual fluxes are given in Table S2.

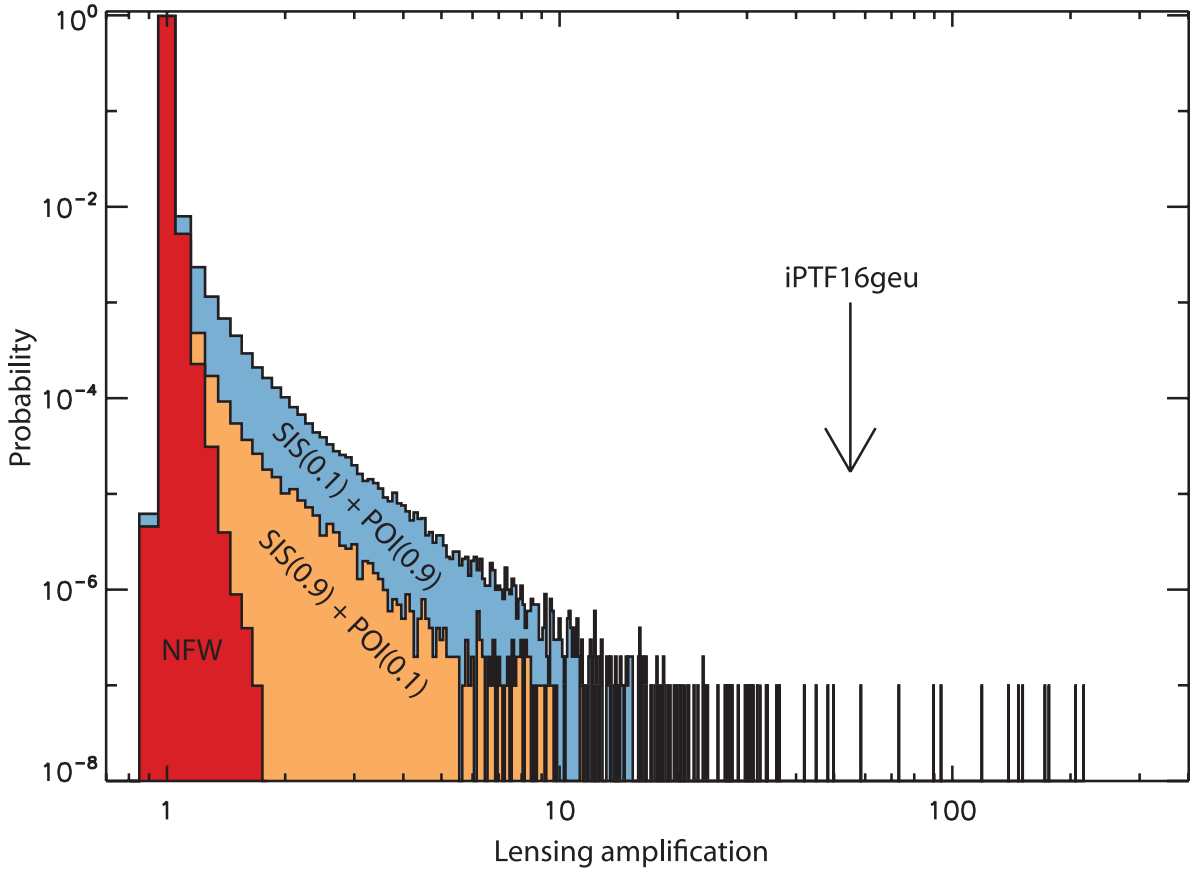

Figure S3: **Computation of the lensing probability for SNe Ia in the Palomar Transient Factory survey.** SNOC simulations (*50*) of the expected likelihood for the gravitational lensing amplification of SNe Ia up to $z = 0.45$ as a function if the density distribution of matter in galaxy halos. The three cases displayed correspond to a smooth NFW profile, and a SIS profile with a 10% and 90% fraction of substructures in the form of point-like lenses (POI). Only simulations with substructures provide non-vanishing probability of finding an event with as high amplification as iPTF16geu, indicted by the arrow.

References

1. A. Goobar, B. Leibundgut, Supernova cosmology: Legacy and future. *Annu. Rev. Nucl. Part. Sci.* **61**, 251–279 (2011). doi:10.1146/annurev-nucl-102010-130434

2. T. S. Kolatt, M. Bartelmann, Gravitational lensing of type Ia supernovae by galaxy clusters. *Mon. Not. R. Astron. Soc.* **296**, 763–772 (1998). doi:10.1046/j.1365-8711.1998.01466.x

3. M. Oguri, Y. Kawano, Gravitational lens time delays for distant supernovae: Breaking the degeneracy between radial mass profiles and the Hubble constant. *Mon. Not. R. Astron. Soc.* **338**, L25–L29 (2003). doi:10.1046/j.1365-8711.2003.06290.x

4. E. E. Falco, M. V. Gorenstein, I. I. Shapiro, On model-dependent bounds on H(0) from gravitational images: Application of Q0957 + 561A,B. *Astrophys. J.* **289**, L1 (1985). doi:10.1086/184422

5. P. Schneider, D. Sluse, Mass-sheet degeneracy, power-law models and external convergence: Impact on the determination of the Hubble constant from gravitational lensing. *Astron. Astrophys.* **559**, A37 (2013). doi:10.1051/0004-6361/201321882

6. R. M. Quimby, M. C. Werner, M. Oguri, S. More, A. More, M. Tanaka, K. Nomoto, T. J. Moriya, G. Folatelli, K. Maeda, M. Bersten, Extraordinary magnification of the ordinary type Ia supernova PS1-10afx. *Astrophys. J.* **768**, L20 (2013). doi:10.1088/2041-8205/768/1/L20

7. R. M. Quimby, M. Oguri, A. More, S. More, T. J. Moriya, M. C. Werner, M. Tanaka, G. Folatelli, M. C. Bersten, K. Maeda, K. Nomoto, Detection of the gravitational lens magnifying a type Ia supernova. *Science* **344**, 396–399 (2014). doi:10.1126/science.1250903 Medline

8. R. Chornock, E. Berger, A. Rest, D. Milisavljevic, R. Lunnan, R. J. Foley, A. M. Soderberg, S. J. Smartt, A. J. Burgasser, P. Challis, L. Chomiuk, I. Czekala, M. Drout, W. Fong, M. E. Huber, R. P. Kirshner, C. Leibler, B. McLeod, G. H. Marion, G. Narayan, A. G. Riess, K. C. Roth, N. E. Sanders, D. Scolnic, K. Smith, C. W. Stubbs, J. L. Tonry, S. Valenti, W. S. Burgett, K. C. Chambers, K. W. Hodapp, N. Kaiser, R.-P. Kudritzki, E. A. Magnier, P. A. Price, PS1-10afx at z = 1.388: Pan-STARRS1 discovery of a new type of superluminous supernova. *Astrophys. J.* **767**, 162 (2013). doi:10.1088/0004-637X/767/2/162

9. P. L. Kelly, S. A. Rodney, T. Treu, R. J. Foley, G. Brammer, K. B. Schmidt, A. Zitrin, A. Sonnenfeld, L.-G. Strolger, O. Graur, A. V. Filippenko, S. W. Jha, A. G. Riess, M. Bradac, B. J. Weiner, D. Scolnic, M. A. Malkan, A. von der Linden, M. Trenti, J. Hjorth, R. Gavazzi, A. Fontana, J. C. Merten, C. McCully, T. Jones, M. Postman, A. Dressler, B. Patel, S. B. Cenko, M. L. Graham, B. E. Tucker, Multiple images of a highly magnified supernova formed by an early-type cluster galaxy lens. *Science* **347**, 1123–1126 (2015). doi:10.1126/science.aaa3350 Medline

10. S. Refsdal, On the possibility of determining Hubble's parameter and the masses of galaxies from the gravitational lens effect. *Mon. Not. R. Astron. Soc.* **128**, 307–310 (1964). doi:10.1093/mnras/128.4.307

11. A. Goobar, E. Mörtsell, R. Amanullah, P. Nugent, Cosmological parameters from lensed supernovae. *Astron. Astrophys.* **393**, 25–32 (2002). doi:10.1051/0004-6361:20020987

12. S. H. Suyu, M. W. Auger, S. Hilbert, P. J. Marshall, M. Tewes, T. Treu, C. D. Fassnacht, L. V. E. Koopmans, D. Sluse, R. D. Blandford, F. Courbin, G. Meylan, Two accurate time-delay distances from strong lensing: Implications for cosmology. *Astrophys. J.* **766**, 70 (2013). doi:10.1088/0004-637X/766/2/70

13. Y. Cao, P. E. Nugent, M. M. Kasliwal, Intermediate Palomar Transient Factory: Realtime image subtraction pipeline. *Publ. Astron. Soc. Pac.* **128**, 114502 (2016). doi:10.1088/1538-3873/128/969/114502

14. N. M. Law, S. R. Kulkarni, R. G. Dekany, E. O. Ofek, R. M. Quimby, P. E. Nugent, J. Surace, C. C. Grillmair, J. S. Bloom, M. M. Kasliwal, L. Bildsten, T. Brown, S. B. Cenko, D. Ciardi, E. Croner, S. G. Djorgovski, J. van Eyken, A. V. Filippenko, D. B. Fox, A. Gal-Yam, D. Hale, N. Hamam, G. Helou, J. Henning, D. A. Howell, J. Jacobsen, R. Laher, S. Mattingly, D. McKenna, A. Pickles, D. Poznanski, G. Rahmer, A. Rau, W. Rosing, M. Shara, R. Smith, D. Starr, M. Sullivan, V. Velur, R. Walters, J. Zolkower, The Palomar Transient Factory: System overview, performance, and first results. *Publ. Astron. Soc. Pac.* **121**, 1395–1408 (2009). doi:10.1086/648598

15. A. Goobar, Detection of a highly magnified type Ia supernova by the intermediate Palomar Transient Factory. *Astron. Telegr.* **9603**, 1 (2016); www.astronomerstelegram.org/?read=9603.

16. A. Ritter, C. C. Ngeow, N. Konidaris, R. Quimby, S. Ben-Ami, The SED Machine—Fast classification of transient objects. *Contrib. Astron. Observ. Skalnate Pleso* **43**, 209–215 (2014). www.astro.sk/caosp/Eedition/FullTexts/vol43no3/pp209-215.pdf

17. J. Guy, P. Astier, S. Baumont, D. Hardin, R. Pain, N. Regnault, S. Basa, R. G. Carlberg, A. Conley, S. Fabbro, D. Fouchez, I. M. Hook, D. A. Howell, K. Perrett, C. J. Pritchet, J. Rich, M. Sullivan, P. Antilogus, E. Aubourg, G. Bazin, J. Bronder, M. Filiol, N. Palanque-Delabrouille, P. Ripoche, V. Ruhlmann-Kleider, SALT2: Using distant supernovae to improve the use of type Ia supernovae as distance indicators. *Astron. Astrophys.* **466**, 11–21 (2007). doi:10.1051/0004-6361:20066930

18. M. M. Phillips, The absolute magnitudes of Type IA supernovae. *Astrophys. J.* **413**, L105 (1993). doi:10.1086/186970

19. R. Tripp, A two-parameter luminosity correction for Type IA supernovae. *Astron. Astrophys.* **331**, 815–820 (1998).

20. M. Betoule, R. Kessler, J. Guy, J. Mosher, D. Hardin, R. Biswas, P. Astier, P. El-Hage, M. Konig, S. Kuhlmann, J. Marriner, R. Pain, N. Regnault, C. Balland, B. A. Bassett, P. J. Brown, H. Campbell, R. G. Carlberg, F. Cellier-Holzem, D. Cinabro, A. Conley, C. B. D'Andrea, D. L. DePoy, M. Doi, R. S. Ellis, S. Fabbro, A. V. Filippenko, R. J. Foley, J. A. Frieman, D. Fouchez, L. Galbany, A. Goobar, R. R. Gupta, G. J. Hill, R. Hlozek, C. J. Hogan, I. M. Hook, D. A. Howell, S. W. Jha, L. Le Guillou, G. Leloudas, C. Lidman, J. L. Marshall, A. Möller, A. M. Mourão, J. Neveu, R. Nichol, M. D. Olmstead, N. Palanque-Delabrouille, S. Perlmutter, J. L. Prieto, C. J. Pritchet, M. Richmond, A. G. Riess, V. Ruhlmann-Kleider, M. Sako, K. Schahmaneche, D. P. Schneider, M. Smith, J. Sollerman, M. Sullivan, N. A. Walton, C. J. Wheeler, Improved cosmological constraints from a joint analysis of the SDSS-II and SNLS supernova samples. *Astron. Astrophys.* **568**, A22 (2014). doi:10.1051/0004-6361/201423413

21. S. Alam, F. D. Albareti, C. Allende Prieto, F. Anders, S. F. Anderson, T. Anderton, B. H. Andrews, E. Armengaud, É. Aubourg, S. Bailey, S. Basu, J. E. Bautista, R. L. Beaton, T. C. Beers, C. F. Bender, A. A. Berlind, F. Beutler, V. Bhardwaj, J. C. Bird, D. Bizyaev, C. H. Blake, M. R. Blanton, M. Blomqvist, J. J. Bochanski, A. S. Bolton, J. Bovy, A. S. Bradley, W. N. Brandt, D. E. Brauer, J. Brinkmann, P. J. Brown, J. R. Brownstein, A. Burden, E. Burtin, N. G. Busca, Z. Cai, D. Capozzi, A. C. Rosell, M. A. Carr, R. Carrera, K. C. Chambers, W. J. Chaplin, Y.-C. Chen, C. Chiappini, S. D. Chojnowski, C.-H. Chuang, N. Clerc, J. Comparat, K. Covey, R. A. C. Croft, A. J. Cuesta, K. Cunha, L. N. Costa, N. D. Rio, J. R. A. Davenport, K. S. Dawson, N. D. Lee, T. Delubac, R. Deshpande, S. Dhital, L. Dutra-Ferreira, T. Dwelly, A. Ealet, G. L. Ebelke, E. M. Edmondson, D. J. Eisenstein, T. Ellsworth, Y. Elsworth, C. R. Epstein, M. Eracleous, S. Escoffier, M. Esposito, M. L. Evans, X. Fan, E. Fernández-Alvar, D. Feuillet, N. F. Ak, H. Finley, A. Finoguenov, K. Flaherty, S. W. Fleming, A. Font-Ribera, J. Foster, P. M. Frinchaboy, J. G. Galbraith-Frew, R. A. García, D. A. García-Hernández, A. E. G. Pérez, P. Gaulme, J. Ge, R. Génova-Santos, A. Georgakakis, L. Ghezzi, B. A. Gillespie, L. Girardi, D. Goddard, S. G. A. Gontcho, J. I. G. Hernández, E. K. Grebel, P. J. Green, J. N. Grieb, N. Grieves, J. E. Gunn, H. Guo, P. Harding, S. Hasselquist, S. L. Hawley, M. Hayden, F. R. Hearty, S. Hekker, S. Ho, D. W. Hogg, K. Holley-Bockelmann, J. A. Holtzman, K. Honscheid, D. Huber, J. Huehnerhoff, I. I. Ivans, L. Jiang, J. A. Johnson, K. Kinemuchi, D. Kirkby, F. Kitaura, M. A. Klaene, G. R. Knapp, J.-P. Kneib, X. P. Koenig, C. R. Lam, T.-W. Lan, D. Lang, P. Laurent, J.-M. L. Goff, A. Leauthaud, K.-G. Lee, Y. S. Lee, T. C. Licquia, J. Liu, D. C. Long, M. López-Corredoira, D. Lorenzo-Oliveira, S. Lucatello, B. Lundgren, R. H. Lupton, C. E. M. Iii, S. Mahadevan, M. A. G. Maia, S. R. Majewski, E. Malanushenko, V. Malanushenko, A. Manchado, M. Manera, Q. Mao, C. Maraston, R. C. Marchwinski, D. Margala, S. L. Martell, M. Martig, K. L. Masters, S. Mathur, C. K. McBride, P. M. McGehee, I. D. McGreer, R. G. McMahon, B. Ménard, M.-L. Menzel, A. Merloni, S. Mészáros, A. A. Miller, J. Miralda-Escudé, H. Miyatake, A. D. Montero-Dorta, S. More, E. Morganson, X. Morice-Atkinson, H. L. Morrison, B. Mosser, D. Muna, A. D. Myers, K.

Nandra, J. A. Newman, M. Neyrinck, D. C. Nguyen, R. C. Nichol, D. L. Nidever, P. Noterdaeme, S. E. Nuza, J. E. O'Connell, R. W. O'Connell, R. O'Connell, R. L. C. Ogando, M. D. Olmstead, A. E. Oravetz, D. J. Oravetz, K. Osumi, R. Owen, D. L. Padgett, N. Padmanabhan, M. Paegert, N. Palanque-Delabrouille, K. Pan, J. K. Parejko, I. Pâris, C. Park, P. Pattarakijwanich, M. Pellejero-Ibanez, J. Pepper, W. J. Percival, I. Pérez-Fournon, I. Pérez-Ràfols, P. Petitjean, M. M. Pieri, M. H. Pinsonneault, G. F. P. Mello, F. Prada, A. Prakash, A. M. Price-Whelan, P. Protopapas, M. J. Raddick, M. Rahman, B. A. Reid, J. Rich, H.-W. Rix, A. C. Robin, C. M. Rockosi, T. S. Rodrigues, S. Rodríguez-Torres, N. A. Roe, A. J. Ross, N. P. Ross, G. Rossi, J. J. Ruan, J. A. Rubiño-Martín, E. S. Rykoff, S. Salazar-Albornoz, M. Salvato, L. Samushia, A. G. Sánchez, B. Santiago, C. Sayres, R. P. Schiavon, D. J. Schlegel, S. J. Schmidt, D. P. Schneider, M. Schultheis, A. D. Schwope, C. G. Scóccola, C. Scott, K. Sellgren, H.-J. Seo, A. Serenelli, N. Shane, Y. Shen, M. Shetrone, Y. Shu, V. S. Aguirre, T. Sivarani, M. F. Skrutskie, A. Slosar, V. V. Smith, F. Sobreira, D. Souto, K. G. Stassun, M. Steinmetz, D. Stello, M. A. Strauss, A. Streblyanska, N. Suzuki, M. E. C. Swanson, J. C. Tan, J. Tayar, R. C. Terrien, A. R. Thakar, D. Thomas, N. Thomas, B. A. Thompson, J. L. Tinker, R. Tojeiro, N. W. Troup, M. Vargas-Magaña, J. A. Vazquez, L. Verde, M. Viel, N. P. Vogt, D. A. Wake, J. Wang, B. A. Weaver, D. H. Weinberg, B. J. Weiner, M. White, J. C. Wilson, J. P. Wisniewski, W. M. Wood-Vasey, C. Ye'che, D. G. York, N. L. Zakamska, O. Zamora, G. Zasowski, I. Zehavi, G.-B. Zhao, Z. Zheng, X. Zhou, Z. Zhou, H. Zou, G. Zhu, The eleventh and twelfth data releases of the Sloan Digital Sky Survey: Final data from SDSS-III. *Astrophys. J. Suppl. Ser.* **219**, 12 (2015). doi:10.1088/0067-0049/219/1/12

22. P. A. Mazzali, M. Sullivan, S. Hachinger, R. S. Ellis, P. E. Nugent, D. A. Howell, A. Gal-Yam, K. Maguire, J. Cooke, R. Thomas, K. Nomoto, E. S. Walker, Hubble Space Telescope spectra of the Type Ia supernova SN 2011fe: A tail of low-density, high-velocity material with Z < Z. *Mon. Not. R. Astron. Soc.* **439**, 1959–1979 (2014). doi:10.1093/mnras/stu077

23. J. A. Cardelli, G. C. Clayton, J. S. Mathis, The relationship between infrared, optical, and ultraviolet extinction. *Astrophys. J.* **345**, 245 (1989). doi:10.1086/167900

24. See supplementary materials.

25. A. Kassiola, I. Kovner, in *Liege International Astrophysical Colloquia, vol. 31*, J. Surdej, D. Fraipont-Caro, E. Gosset, S. Refsdal, M. Remy, Eds. (1993), p. 571.

26. R. Kormann, P. Schneider, M. Bartelmann, Isothermal elliptical gravitational lens models. *Astron. Astrophys.* **284**, 285 (1994).

27. R. Kayser, S. Refsdal, Detectability of gravitational microlensing in the quasar QS02237+0305. *Nature* **338**, 745–746 (1989). doi:10.1038/338745a0

28. H. J. Witt, S. Mao, Interpretation of microlensing events in Q2237 + 0305. *Astrophys. J.* **429**, 66 (1994). doi:10.1086/174302

29. M. Oguri, P. J. Marshall, Gravitationally lensed quasars and supernovae in future wide-field optical imaging surveys. *Mon. Not. R. Astron. Soc.* **405**, 2579–2593 (2010). doi:10.1111/j.1365-2966.2010.16639.x

30. K.-H. Chae, The Cosmic Lens All-Sky Survey: Statistical strong lensing, cosmological parameters, and global properties of galaxy populations. *Mon. Not. R. Astron. Soc.* **346**, 746–772 (2003). doi:10.1111/j.1365-2966.2003.07092.x

31. L. A. Moustakas, J. Brownstein, R. Fadely, C. D. Fassnacht, R. Gavazzi, T. Goodsall, R. L. Griffith, C. R. Keeton, J. P. Kneib, A. Koekemoer, L. V. E. Koopmans, P. J. Marshall, J. Merten, R. B. Metcalf, M. Oguri, C. Papovich, H. Rein, R. Ryan, K. R. Stewart, T. Treu, The Orphan Lenses Project. *Am. Astron. Soc. Meet. Abstr.* **219**, 146.01 (2012).

32. D. A. Goldstein, P. E. Nugent, How to find gravitationally lensed type Ia supernovae. *Astrophys. J.* **834**, L5 (2017). doi:10.3847/2041-8213/834/1/L5

33. O. Yaron, A. Gal-Yam, WISeREP—An interactive supernova data repository. *Publ. Astron. Soc. Pac.* **124**, 668–681 (2012). doi:10.1086/666656

34. More information about the iPTF survey is available at www.ptf.caltech.edu/iptf.

35. E. O. Ofek, R. Laher, J. Surace, D. Levitan, B. Sesar, A. Horesh, N. Law, J. C. van Eyken, S. R. Kulkarni, T. A. Prince, P. Nugent, M. Sullivan, O. Yaron, A. Pickles, M. Agüeros, I. Arcavi, L. Bildsten, J. Bloom, S. B. Cenko, A. Gal-Yam, C. Grillmair, G. Helou, M. M. Kasliwal, D. Poznanski, R. Quimby, The Palomar Transient Factory photometric catalog 1.0. *Publ. Astron. Soc. Pac.* **124**, 854–860 (2012). doi:10.1086/666978

36. H. Brink, J. W. Richards, D. Poznanski, J. S. Bloom, J. Rice, S. Negahban, M. Wainwright, Using machine learning for discovery in synoptic survey imaging data. *Mon. Not. R. Astron. Soc.* **435**, 1047–1060 (2013). doi:10.1093/mnras/stt1306

37. U. Rebbapragada, B. Bue, P. R. Wozniak, Time-domain surveys and data shift: Case study at the intermediate Palomar Transient Factory. *Am. Astron. Soc. Meet. Abstr.* **225**, 434.02 (2015).

38. F. J. Masci, R. R. Laher, U. D. Rebbapragada, G. B. Doran, A. A. Miller, E. Bellm, M. Kasliwal, E. O. Ofek, J. Surace, D. L. Shupe, C. J. Grillmair, E. Jackson, T. Barlow, L. Yan, Y. Cao, S. B. Cenko, L. J. Storrie-Lombardi, G. Helou, T. A. Prince, S. R. Kulkarni, The IPAC image subtraction and discovery pipeline for the intermediate Palomar Transient Factory. *Publ. Astron. Soc. Pac.* **129**, 014002 (2017). doi:10.1088/1538-3873/129/971/014002

39. C. Fremling, J. Sollerman, F. Taddia, M. Ergon, M. Fraser, E. Karamehmetoglu, S. Valenti, A. Jerkstrand, I. Arcavi, F. Bufano, N. Elias Rosa, A. V. Filippenko, D. Fox, A. Gal-Yam, D. A. Howell, R. Kotak, P. Mazzali, D. Milisavljevic, P. E. Nugent, A. Nyholm, E. Pian, S. Smartt, PTF12os and iPTF13bvn. *Astron. Astrophys.* **593**, A68 (2016). doi:10.1051/0004-6361/201628275

40. J. B. Oke, J. E. Gunn, An efficient low resolution and moderate resolution spectrograph for the Hale Telescope. *Publ. Astron. Soc. Pac.* **94**, 586 (1982). doi:10.1086/131027

41. W. Freudling, M. Romaniello, D. M. Bramich, P. Ballester, V. Forchi, C. E. García-Dabló, S. Moehler, M. J. Neeser, Automated data reduction workflows for astronomy. *Astron. Astrophys.* **559**, A96 (2013). doi:10.1051/0004-6361/201322494

42. J. Larkin, M. Barczys, A. Krabbe, S. Adkins, T. Aliado, P. Amico, G. Brims, R. Campbell, J. Canfield, T. Gasaway, A. Honey, C. Iserlohe, C. Johnson, E. Kress, D. LaFreniere, J. Lyke, K. Magnone, N. Magnone, M. McElwain, J. Moon, A. Quirrenbach, G. Skulason, I. Song, M. Spencer, J. Weiss, S. Wright, OSIRIS: A diffraction limited integral field spectrograph for Keck. *Proc. SPIE* **6269**, 62691A (2006).

43. J. L. Sérsic, Influence of the atmospheric and instrumental dispersion on the brightness distribution in a galaxy. *Bol. Asoc. Argentina Astron. La Plata Argentina* **6**, 41 (1963).

44. R. Amanullah, J. Johansson, A. Goobar, R. Ferretti, S. Papadogiannakis, T. Petrushevska, P. J. Brown, Y. Cao, C. Contreras, H. Dahle, N. Elias-Rosa, J. P. U. Fynbo, J. Gorosabel, L. Guaita, L. Hangard, D. A. Howell, E. Y. Hsiao, E. Kankare, M. Kasliwal, G. Leloudas, P. Lundqvist, S. Mattila, P. Nugent, M. M. Phillips, A. Sandberg, V. Stanishev, M. Sullivan, F. Taddia, G. Östlin, S. Asadi, R. Herrero-Illana, J. J. Jensen, K. Karhunen, S. Lazarevic, E. Varenius, P. Santos, S. S. Sridhar, S. H. J. Wallström, J. Wiegert, Diversity in extinction laws of Type Ia supernovae measured between 0.2 and 2 μm. *Mon. Not. R. Astron. Soc.* **453**, 3300 (2015). doi:10.1093/mnras/stv1505

45. P. A. R. Ade, N. Aghanim, M. Arnaud, M. Ashdown, J. Aumont, C. Baccigalupi, A. J. Banday, R. B. Barreiro, J. G. Bartlett, N. Bartolo, E. Battaner, R. Battye, K. Benabed, A. Benoît, A. Benoit-Lévy, J.-P. Bernard, M. Bersanelli, P. Bielewicz, J. J. Bock, A. Bonaldi, L. Bonavera, J. R. Bond, J. Borrill, F. R. Bouchet, F. Boulanger, M. Bucher, C. Burigana, R. C. Butler, E. Calabrese, J.-F. Cardoso, A. Catalano, A. Challinor, A. Chamballu, R.-R. Chary, H. C. Chiang, J. Chluba, P. R. Christensen, S. Church, D. L. Clements, S. Colombi, L. P. L. Colombo, C. Combet, A. Coulais, B. P. Crill, A. Curto, F. Cuttaia, L. Danese, R. D. Davies, R. J. Davis, P. de Bernardis, A. de Rosa, G. de Zotti, J. Delabrouille, F.-X. Désert, E. Di Valentino, C. Dickinson, J. M. Diego, K. Dolag, H. Dole, S. Donzelli, O. Doré, M. Douspis, A. Ducout, J. Dunkley, X. Dupac, G. Efstathiou, F. Elsner, T. A. Enßlin, H. K. Eriksen, M. Farhang, J. Fergusson, F. Finelli, O. Forni, M. Frailis, A. A. Fraisse, E. Franceschi, A. Frejsel, S. Galeotta, S. Galli, K. Ganga, C. Gauthier, M. Gerbino, T. Ghosh, M. Giard, Y. Giraud-Héraud, E. Giusarma, E. Gjerløw, J. González-Nuevo, K. M. Górski, S. Gratton, A. Gregorio, A. Gruppuso, J. E. Gudmundsson, J. Hamann, F. K. Hansen, D. Hanson, D. L. Harrison, G. Helou, S. Henrot-Versillé, C. Hernández-Monteagudo, D. Herranz, S. R. Hildebrandt, E. Hivon, M. Hobson, W. A. Holmes, A. Hornstrup, W. Hovest, Z. Huang, K. M. Huffenberger, G. Hurier, A. H. Jaffe, T. R. Jaffe, W. C. Jones, M. Juvela, E. Keihänen, R. Keskitalo, T. S. Kisner, R. Kneissl, J. Knoche, L. Knox, M. Kunz, H. Kurki-Suonio, G. Lagache, A. Lähteenmäki, J.-M. Lamarre, A. Lasenby, M. Lattanzi,

C. R. Lawrence, J. P. Leahy, R. Leonardi, J. Lesgourgues, F. Levrier, A. Lewis, M. Liguori, P. B. Lilje, M. Linden-Vørnle, M. López-Caniego, P. M. Lubin, J. F. Macías-Pérez, G. Maggio, D. Maino, N. Mandolesi, A. Mangilli, A. Marchini, M. Maris, P. G. Martin, M. Martinelli, E. Martínez-González, S. Masi, S. Matarrese, P. McGehee, P. R. Meinhold, A. Melchiorri, J.-B. Melin, L. Mendes, A. Mennella, M. Migliaccio, M. Millea, S. Mitra, M.-A. Miville-Deschênes, A. Moneti, L. Montier, G. Morgante, D. Mortlock, A. Moss, D. Munshi, J. A. Murphy, P. Naselsky, F. Nati, P. Natoli, C. B. Netterfield, H. U. Nørgaard-Nielsen, F. Noviello, D. Novikov, I. Novikov, C. A. Oxborrow, F. Paci, L. Pagano, F. Pajot, R. Paladini, D. Paoletti, B. Partridge, F. Pasian, G. Patanchon, T. J. Pearson, O. Perdereau, L. Perotto, F. Perrotta, V. Pettorino, F. Piacentini, M. Piat, E. Pierpaoli, D. Pietrobon, S. Plaszczynski, E. Pointecouteau, G. Polenta, L. Popa, G. W. Pratt, G. Prézeau, S. Prunet, J.-L. Puget, J. P. Rachen, W. T. Reach, R. Rebolo, M. Reinecke, M. Remazeilles, C. Renault, A. Renzi, I. Ristorcelli, G. Rocha, C. Rosset, M. Rossetti, G. Roudier, B. Rouillé d'Orfeuil, M. Rowan-Robinson, J. A. Rubiño-Martín, B. Rusholme, N. Said, V. Salvatelli, L. Salvati, M. Sandri, D. Santos, M. Savelainen, G. Savini, D. Scott, M. D. Seiffert, P. Serra, E. P. S. Shellard, L. D. Spencer, M. Spinelli, V. Stolyarov, R. Stompor, R. Sudiwala, R. Sunyaev, D. Sutton, A.-S. Suur-Uski, J.-F. Sygnet, J. A. Tauber, L. Terenzi, L. Toffolatti, M. Tomasi, M. Tristram, T. Trombetti, M. Tucci, J. Tuovinen, M. Türler, G. Umana, L. Valenziano, J. Valiviita, F. Van Tent, P. Vielva, F. Villa, L. A. Wade, B. D. Wandelt, I. K. Wehus, M. White, S. D. M. White, A. Wilkinson, D. Yvon, A. Zacchei, A. Zonca, *Planck* 2015 results. *Astron. Astrophys.* **594**, A13 (2016). doi:10.1051/0004-6361/201525830

46. C. R. Keeton, Computational methods for gravitational lensing. arxiv:0102340 [astro-ph] (2001).

47. C. R. Keeton, A catalog of mass models for gravitational lensing. arxiv:0102341 [astro-ph] (2001).

48. P. Schneider, J. Ehlers, E. E. Falco, *Gravitational Lenses* (Springer, 1992).

49. R. Pereira, R. C. Thomas, G. Aldering, P. Antilogus, C. Baltay, S. Benitez-Herrera, S. Bongard, C. Buton, A. Canto, F. Cellier-Holzem, J. Chen, M. Childress, N. Chotard, Y. Copin, H. K. Fakhouri, M. Fink, D. Fouchez, E. Gangler, J. Guy, W. Hillebrandt, E. Y. Hsiao, M. Kerschhaggl, M. Kowalski, M. Kromer, J. Nordin, P. Nugent, K. Paech, R. Pain, E. Pécontal, S. Perlmutter, D. Rabinowitz, M. Rigault, K. Runge, C. Saunders, G. Smadja, C. Tao, S. Taubenberger, A. Tilquin, C. Wu, Spectrophotometric time series of SN 2011fe from the nearby supernova factory. *Astron. Astrophys.* **554**, A27 (2013). doi:10.1051/0004-6361/201221008

50. A. Goobar, E. Mörtsell, R. Amanullah, M. Goliath, L. Bergström, T. Dahlén, SNOC: A Monte-Carlo simulation package for high-*z* supernova observations. *Astron. Astrophys.* **392**, 757–771 (2002). doi:10.1051/0004-6361:20020930

51. J. F. Navarro, C. S. Frenk, S. D. M. White, A universal density profile from hierarchical clustering. *Astrophys. J.* **490**, 493–508 (1997). doi:10.1086/304888

52. V. Springel, J. Wang, M. Vogelsberger, A. Ludlow, A. Jenkins, A. Helmi, J. F. Navarro, C. S. Frenk, S. D. M. White, The Aquarius Project: The subhaloes of galactic haloes. *Mon. Not. R. Astron. Soc.* **391**, 1685–1711 (2008). doi:10.1111/j.1365-2966.2008.14066.x

53. G. Dobler, C. R. Keeton, Microlensing of lensed supernovae. *Astrophys. J.* **653**, 1391–1399 (2006). doi:10.1086/508769

54. P. L. Schechter, D. Pooley, J. A. Blackburne, J. Wambsganss, A calibration of the stellar mass fundamental plane at $z \sim 0.5$ using the micro-lensing-induced flux ratio anomalies of macro-lensed quasars. *Astrophys. J.* **793**, 96 (2014). doi:10.1088/0004-637X/793/2/96

55. J. Wambsganss, Gravitational microlensing. In *Gravitational Lensing: Strong, Weak and Micro*, G. Meylan, P. Jetzer, P. North, Eds. (Springer, 2006), pp. 453–540.

56. S. Ben-Ami, N. Konidaris, R. Quimby, J. T. Davis, C. C. Ngeow, A. Ritter, A. Rudy, The SED machine: A dedicated transient IFU spectrograph. *Proc. SPIE* **8446**, 844686 (2012). doi:10.1117/12.926317